Electronic Supplementary Material (ESI) for Dalton Transactions.
This journal is © The Royal Society of Chemistry 2017

ELECTRONIC SUPPLEMENTARY INFORMATION

Exploring the Localized to Delocalized Transition in Non-Symmetric Bimetallic Ruthenium Polypyridines

Paola S. Oviedo, German E. Pieslinger, Alejandro Cadranel, and Luis M. Baraldo.

Contents	Page
Structural characterization	**S2**
Table S1	S2
Table S2	S3
Figure S1	S3
Figure S2	S4
Cyclic Voltammograms	**S5**
Figure S3	S5
Solvent Dependence of NIR bands	**S6**
Figure S4	S6
Table S3	S7
UV-vis spectroelectrochemistry	**S8**
Figure S5	S8
IR spectroelectrochemistry	**S9**
Figure S6	S9
Figure S7	S9
Figure S8	S10
Theoretical Calculations	**S11**
Figure S9	S11
Figure S10	S11
Figure S11	S12
Figure S12	S12
Table S4	S13
Table S5	S13
Figure S13	S14
Figure S14	S15
Table S6	S16
Figure S15	S17
Figure S16	S18
Table S7	S19
Figure S17	S20
Figure S18	S21
Table S8	S22
Figure S19	S22
Figure S20	S23
Figure S21	S24

Structural Characterization

	4(PF$_6$)$_3$
Empirical Formula	C_{48} H_{38} F_{18} N_{11} P_3 Ru_2
Formula weight	1405.94
T (K)	298 (2)
Crystal system	Triclinic
Space Group	P-1
a (Å)	12.8420(7)
b (Å)	13.5320(11)
c (Å)	19.2627(13)
α (°)	99.836(6)
β (°)	102.202(5)
γ (°)	112.404(6)
V (Å^3)	2905.4(3)
Z	2
D_{calc} (mg/m^3)	1.607
Absorption coefficient (mm^{-1})	0.704
F(000)	1396
λ(Å)	0.7107
θ Range data collection (°)	3.57-26.00
Index ranges	$-15 \leq h \leq 15$
	$-16 \leq k \leq 16$
	$-23 \leq l \leq 23$
Reflections collected/unique	23261/11394
Rint	0.0452
Observed reflections [I>2σ(I)]	7160
Completeness (%)	99.7
Maximum / minimum transmission	1.0000 / 0.65597
Data/restraints/parameters	11394/58/744
Goodness-of-fit (GOF) on F^2	0.983
Final R-index [I>2σ(I)]/ all data	0.0721/0.1110
*w*R index [I>2σ(I)] /all data	0.1996/0.2298
Largest peak and hole (e A^{-3})	-0.999 and 1.245
Weights, *w*	$1/[\sigma^2(F_o^2) + (0.1427P)^2]$ where $P=(Fo^2+2F_c^2)/3$

Table S1. Crystallographic data for **4(PF$_6$)$_3$**

	bond	length, Å			bond	length, Å	
Ligand	**Ru_{tb} moiety**		**DFT**	**Ligand**	**Ru_{b2} moiety**		**DFT**
CN	**Ru_{tb} -C(1)**	1.972	2.017	**NC**	**Ru_{b2}-N(1)**	2.024	2.079
tpy	**Ru_{tb} -N(7)**	2.076	2.107	**$NCCH_3$**	**Ru_{b2}-N(6)**	2.036	2.079
	Ru_{tb} -N(8)	1.970	1.999	**bpy1**	**Ru_{b2}-N(2)**	2.049	2.089
	Ru_{tb} -N(9)	2.065	2.108		**Ru_{b2}-N(3)**	2.052	2.068
bpy	**Ru_{tb} -N(10)**	2.085	2.126	**bpy2**	**Ru_{b2}-N(4)**	2.059	2.079
	Ru_{tb} -N(11)	2.089	2.112		**Ru_{b2}-N(5)**	2.056	2.093
	Bridge						
CN	**C(1)-N(1)**	1.189	1.189				
	angle	**degree**			**angle**	**degree**	
	Ru_{tb} -C(1)-N(1)	175.17	179.47		**Ru_{b2}-N(1)-C(1)**	167.60	178.87

Table S2. Selected Bond Distances and Angles for [**4**]$(PF_6)_3$

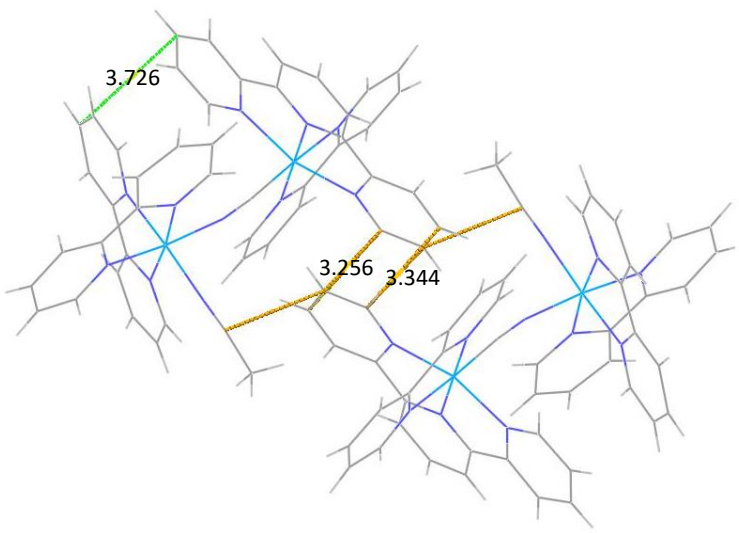

Figure S1. Short contact distances found in the crystal structure of [**4**]$(PF_6)_3$

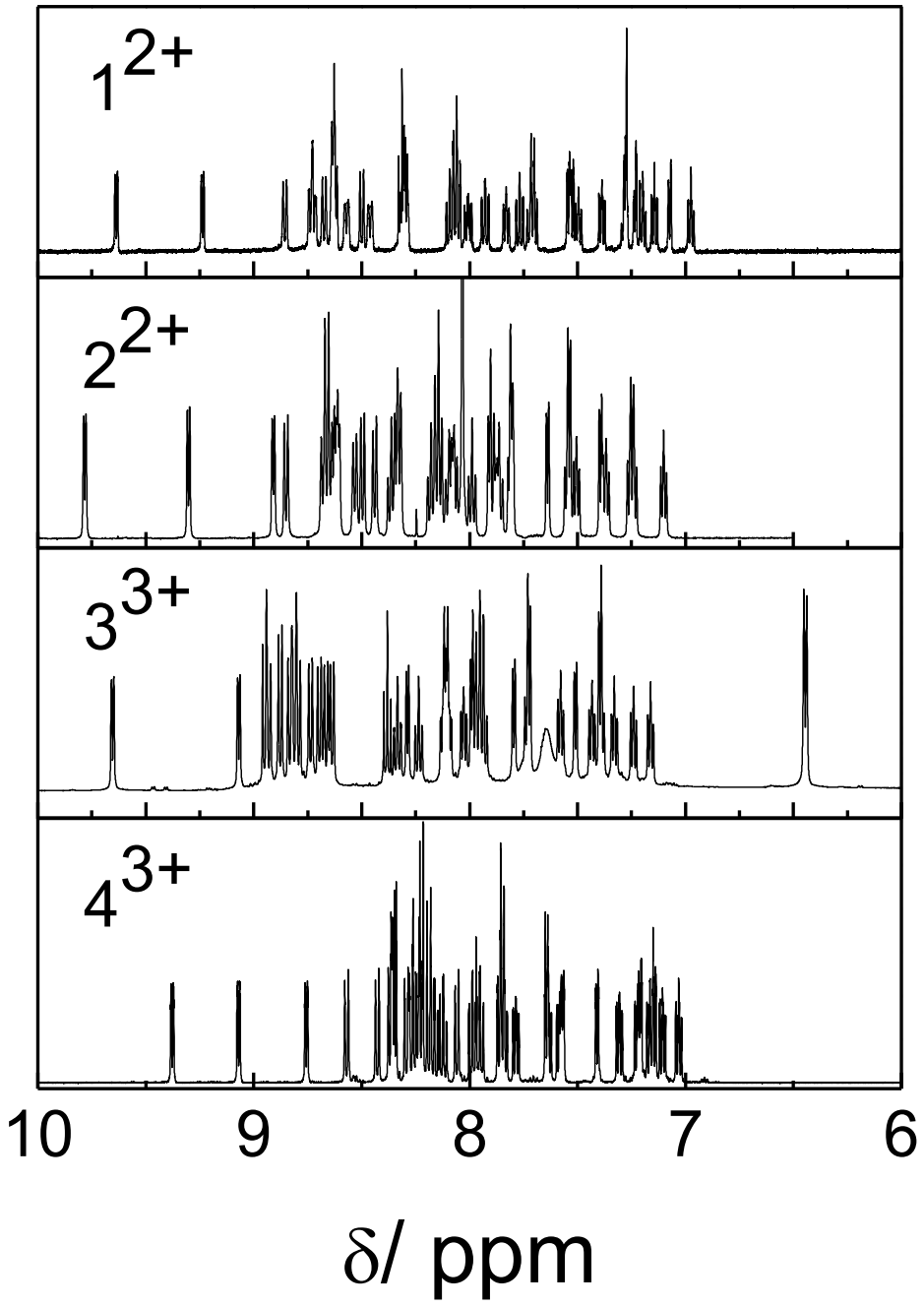

Figure S2. 500 MHz ^{1}H-NMR spectra of complexes [**1**]$(Cl)_2$ (DMSO-d6), [**2**]$(PF_6)_2$ (ACN-d3), [**3**]$(PF_6)_3$ (ACN-d3) and [**4**]$(PF_6)_3$ (ACN-d3), from top to bottom.

Cyclic voltammograms

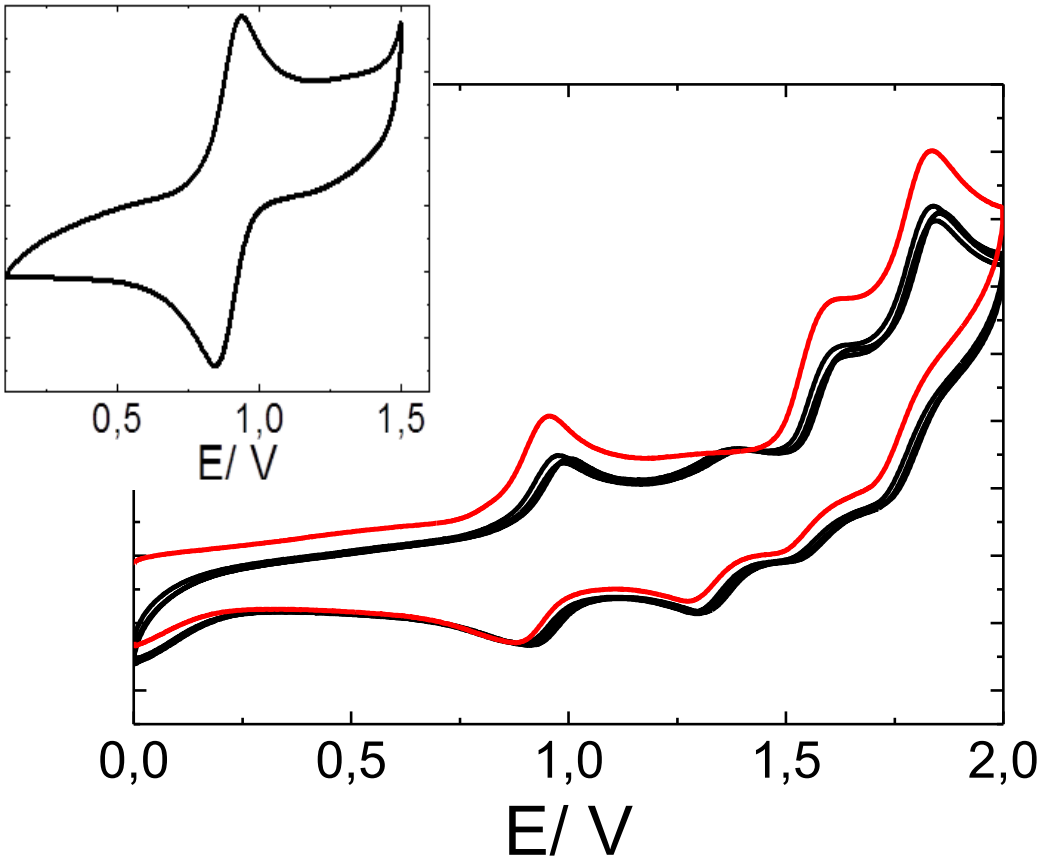

Figure S3. Cyclic voltammogram of **2** in acetonitrile/0.1 M [TBA]PF6 cycling 5 times at 100 mV·s^{-1} scan rate. First cycle is shown in red color. Inset: Cyclic voltammogram of **2** in acetonitrile/0.1 M [TBA]PF6 at 5 mV·s^{-1} scan rate up to 1,5 V.

Solvent Dependence of NIR bands

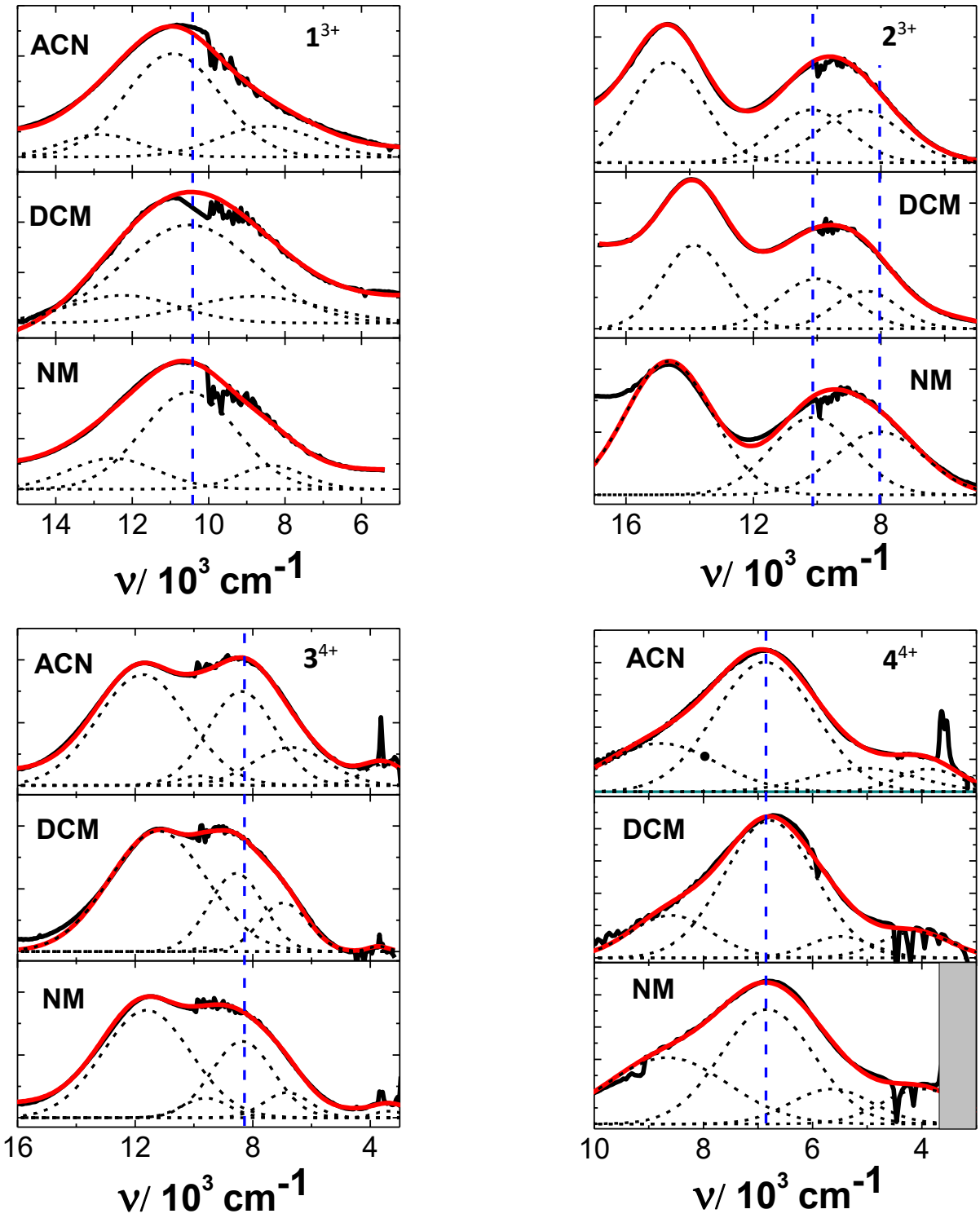

Figure S4. NIR absorption spectra of **1**$^{3+}$ (left panel, top), **2**$^{3+}$ (right panel, top), **3**$^{4+}$ (left panel, bottom) and **4**$^{4+}$ (right panel, bottom) in different solvents: acetonitrile (ACN), dichloromethane (DCM) and nitromethane (NM). Dashed lines result from Gaussian deconvolution with spectral fitting procedures.

complex	ν_{max}/cm^{-1} (ε_{max}/10^3 M^{-1} cm^{-1}) [$\Delta\nu_{1/2}$/10^3 cm^{-1}]		
	ACN	DCM	NM
1^{3+}	8490 (0,6) [3,0]	8806 (0,5) [4,0]	8360 (0,5) [2,0]
	10940 (2,0) [2,9]	10510 (1,9) [4,0]	10500 (1,9) [2,9]
	12840 (0,4) [2,4]	12240 (0,5) [3,7]	12520 (0,6) [2,8]
2^{3+}	8670 (1,7) [3,0]	8470 (1,2) [2,4]	8045 (2,0) [3,3]
	10180 (1,7) [2,8]	10040 (1,6) [2,7]	10140 (2,5) [3,0]
	14690 (3,2) [2,7]	13860 (2,7) [2,4]	14660 (4,3) (3,2)
3^{4+}	3540 (0,7) [1,7]	3160 (1,8) [3,1]	3380 (0,2) [1,2]
	6720 (1,2) [3,0]	6350 (1,7) [2,6]	6825 (0,8) [1,9]
	8385 (3,0) [2,7]	8415 (3,4) [2,9]	8350 (2,4) [2,5]
	9850 (0,3) [1,5]	9970 (0,3) [1,8]	9600 (0,6) [1,9]
	11740 (3,5) [3,6]	11280 (4,0) [3,9]	11610 (3,4) [3,5]
4^{4+}	3880 (1,5) [1,7]	4120 (1,6) [1,5]	3995 (2,2) [1,7]
	5380 (0,3) [1,3]	5495 (1,3) [1,4]	5650 (2,2) [1,8]
	6880 (7,8) [2,3]	6790 (8,5) [2,0]	6830 (7,1) [2,0]
	8795 (2,1) [2,2]	8595 (2,6) [1,7]	8660 (4,1) [2,6]

Table S3. Spectral parameters for deconvoluted NIR bands of mixed-valence species in different solvents: acetonitrile (ACN), dichloromethane (DCM) and nitromethane (NM).

UV-vis spectroelectrochemistry

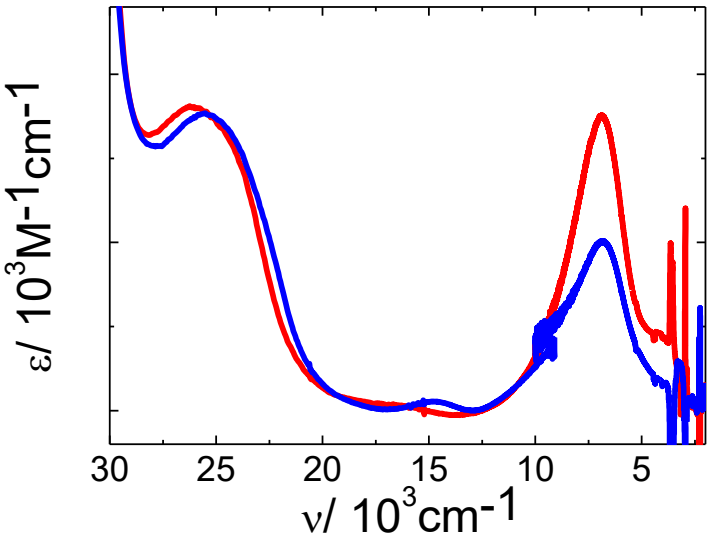

Figure S5. UV-vis-NIR spectrum after first oxidation process of $\mathbf{4}^{3+}$ (red) and second oxidation process of $\mathbf{2}^{2+}$ (blue).

IR spectroelectrochemistry

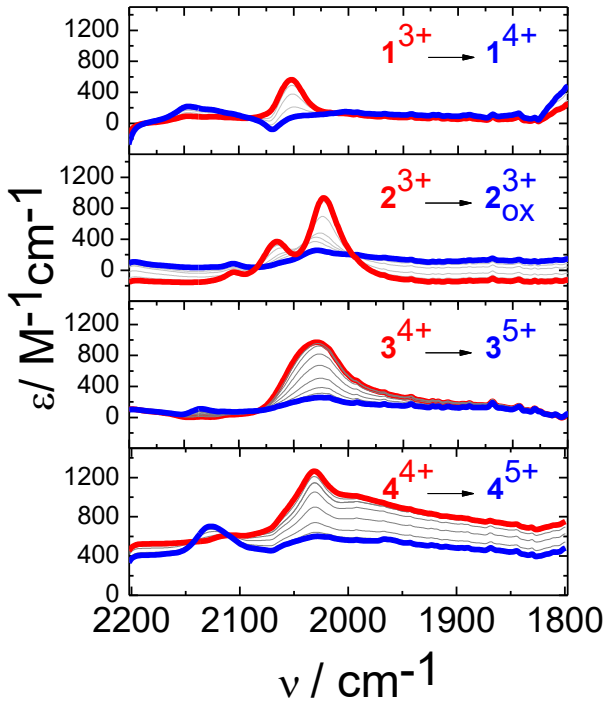

Figure S6. IR spectroelectrochemistry of $\mathbf{1}^{2+}$ (top) to $\mathbf{4}^{3+}$ (bottom) in acetonitrile/0.1 M [TBA]PF_6, during the second oxidation process. The spectra of the [II,III] (red) and [III,III] (blue) species are highlighted.

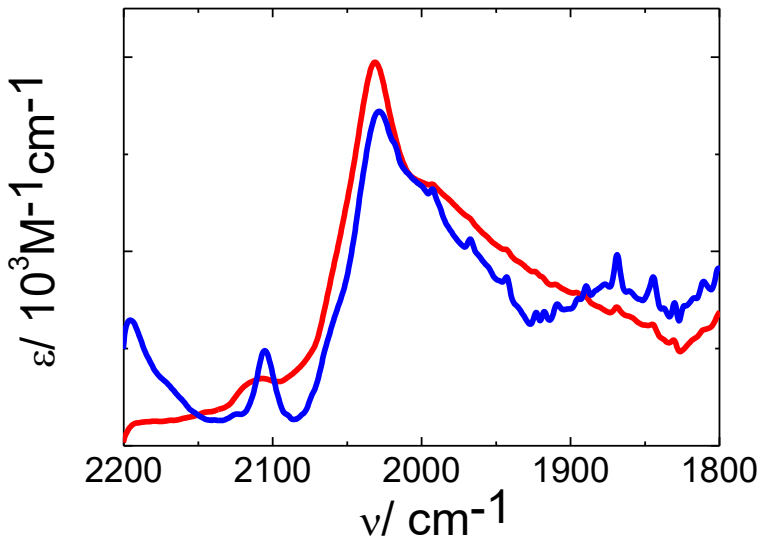

Figure S7. IR spectrum after first oxidation process of $\mathbf{4}^{3+}$ (red) and second oxidation process of $\mathbf{2}^{2+}$ (blue).

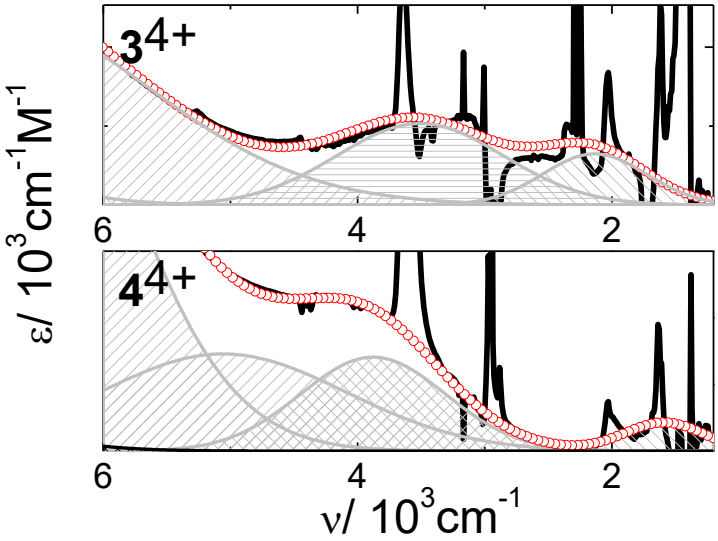

Figure S8. Amplification of the spectra of Figure 4 for the species $\mathbf{4}^{4+}$ and $\mathbf{3}^{4+}$ in the NIR-IR region.

Theoretical Calculations

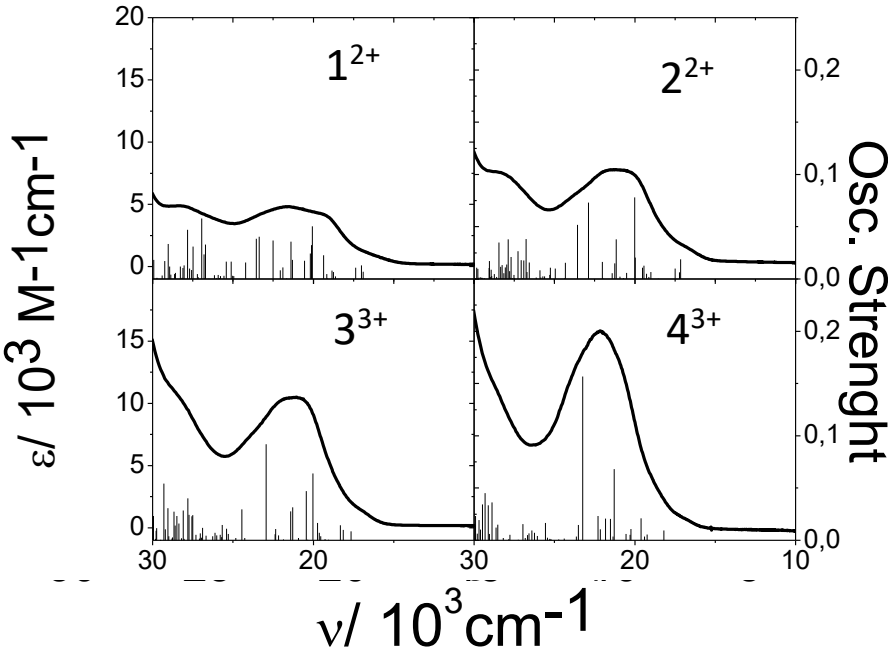

Figure S9. Comparison of the NIR spectra of **1**$^{2+}$ (left, top), **2**$^{2+}$ (right, top), **3**$^{3+}$ (left, bottom) and **4**$^{3+}$ (right, bottom) in acetonitrile/0.1 M [TBA]PF_6 and the energy of the transitions/vibrations predicted by (TD)DFT calculations (bars).

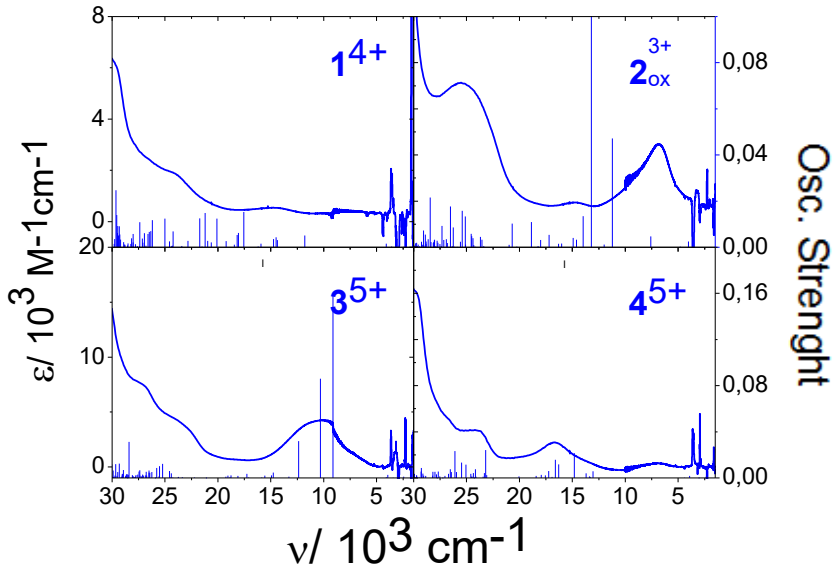

Figure S10. Comparison of the NIR spectra of **1**$^{4+}$ (left, top), **2**$^{4+}$ (right, top), **3**$^{5+}$ (left, bottom) and **4**$^{5+}$ (right, bottom) in acetonitrile/0.1 M [TBA]PF_6 and the energy of the transitions/vibrations predicted by (TD)DFT calculations (bars).

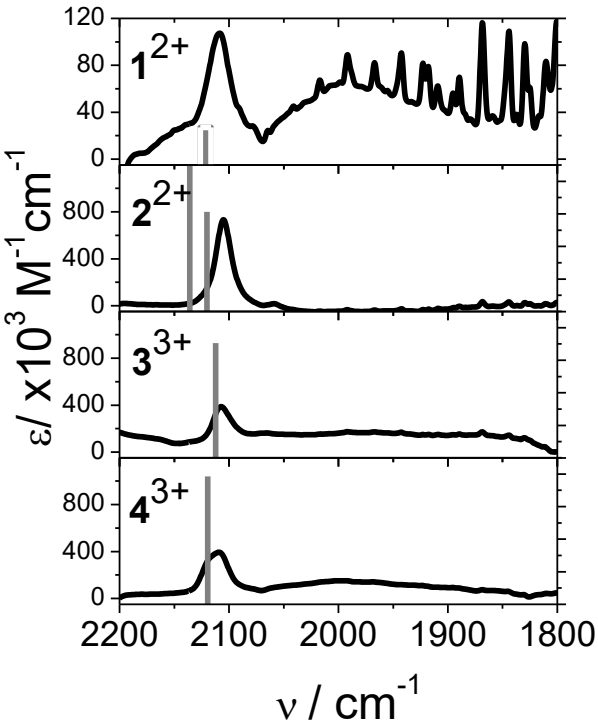

Figure S11. Comparison of the IR spectra of **1**$^{2+}$ (top) to **4**$^{3+}$ (bottom) in acetonitrile/0.1 M [TBA]PF_6 and the energy of the vibrations predicted by the DFT calculations (bars).

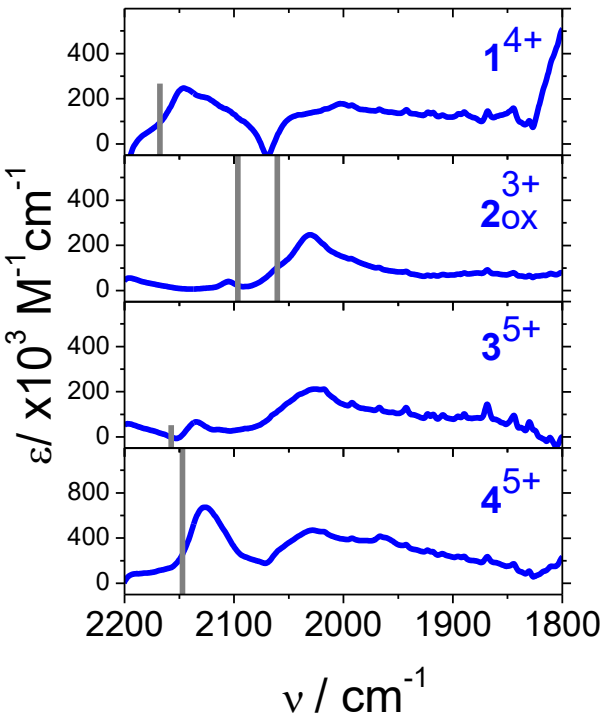

Figure S12. Comparison of the IR spectra of **1**$^{4+}$ (top) to **4**$^{5+}$ (bottom) in acetonitrile/0.1 M [TBA]PF_6 and the energy of the vibrations predicted by the DFT calculations (bars).

Complex	Redox state	*Experimental* ν_{CN} (ε)/cm^{-1} (M^{-1} cm^{-1})	*Calculated* ν_{CN}/cm^{-1} (IR$_{act}$/a.u.)	*Assignment*
1	[II,II]	2109 (110)	2121 (272)	ν_{CN} (brigde)
	[III,II]	2053 (550)	2068 (2869)	ν_{CN} (brigde)
	[III,III]	2147 (230)	2168 (267)	ν_{CN} (brigde)
2	[II,II]	2058 (20) 2105 (730)	2120 (306) 2136 (780)	ν_{CN} (brigde) ν_{CN} (SCN)
	[III,II]	2022 (1060) 2065 (510)	2060 (4636) 2097 (1233)	ν_{CN} (SCN) ν_{CN} (bridge)
	[III,III]	2029 (250) ---	2072 (1583) 2169 (103)	ν_{CN} (brigde) ν_{CN} (SCN)
3	[II,II]	2106 (339)	2112 (352)	ν_{CN} (brigde)
	[III,II]	2021 (1110)	2044 (2452)	ν_{CN} (brigde)
	[III,III]	2135 (110)	2157 (52)	ν_{CN} (brigde)
4	[II,II]	2110 (410) ---	2119 (392) 2321 (16)	ν_{CN} (brigde) ν_{CN} (MeCN)
	[III,II]	2032 (1000) ---	2036 (1010) 2341 (114)	ν_{CN} (brigde) ν_{CN} (MeCN)
	[III,III]	2130 (700) ---	2147 (880) 2341 (189)	ν_{CN} (brigde) ν_{CN} (MeCN)

Table S4. Experimental and calculated IR frequencies for complexes **1** to **4** in their [II,II], [II,III] and [III,III] oxidation states. Experimental measures were done in acetonitrile/0.1 M [TBA]PF6

No.	Energy (cm-1)	Wavelength (nm)	Osc. Strength	Major contribs	Assignment
1	3034	3296	0.0001	H-4(B)->LUMO(B) (41%) H-2(B)->LUMO(B) (29%) H-1(B)->LUMO(B) (11%)	IC
2	3406	2936	0.0007	H-3(B)->LUMO(B) (77%)	IC
3	8245	1213	0.0304	H-1(B)->LUMO(B) (28%) HOMO(B)->LUMO(B) (69%)	IVCT
4	9328	1072	0.1003	H-2(B)->LUMO(B) (29%) H-1(B)->LUMO(B) (47%) HOMO(B)->LUMO(B) (17%)	IVCT+IC
5	10797	926	0.0140	H-4(B)->LUMO(B) (46%) H-2(B)->LUMO(B) (40%) H-1(B)->LUMO(B) (10%)	IVCT+IC
39	24363	410	0.0706	H-2(A)->L+4(A) (15%) H-1(A)->L+3(A) (33%) H-1(B)->L+4(B) (22%)	MLCT

Table S5. Selected electronic transitions of the doublet **1**$^{3+}$ ion calculated in MeCN.

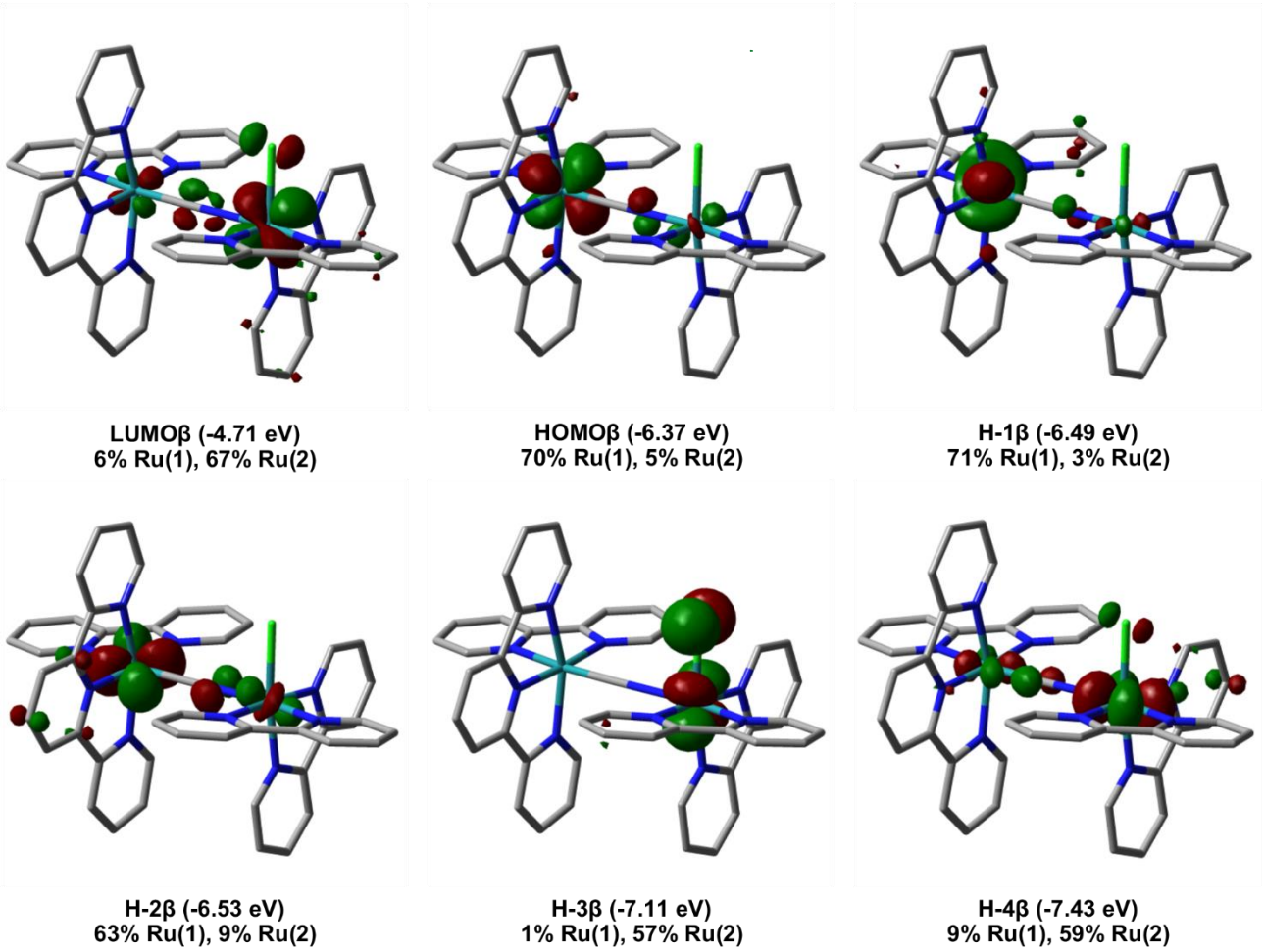

Figure S13. Computed molecular orbitals for the doublet $\mathbf{1}^{3+}$ ion calculated in MeCN.

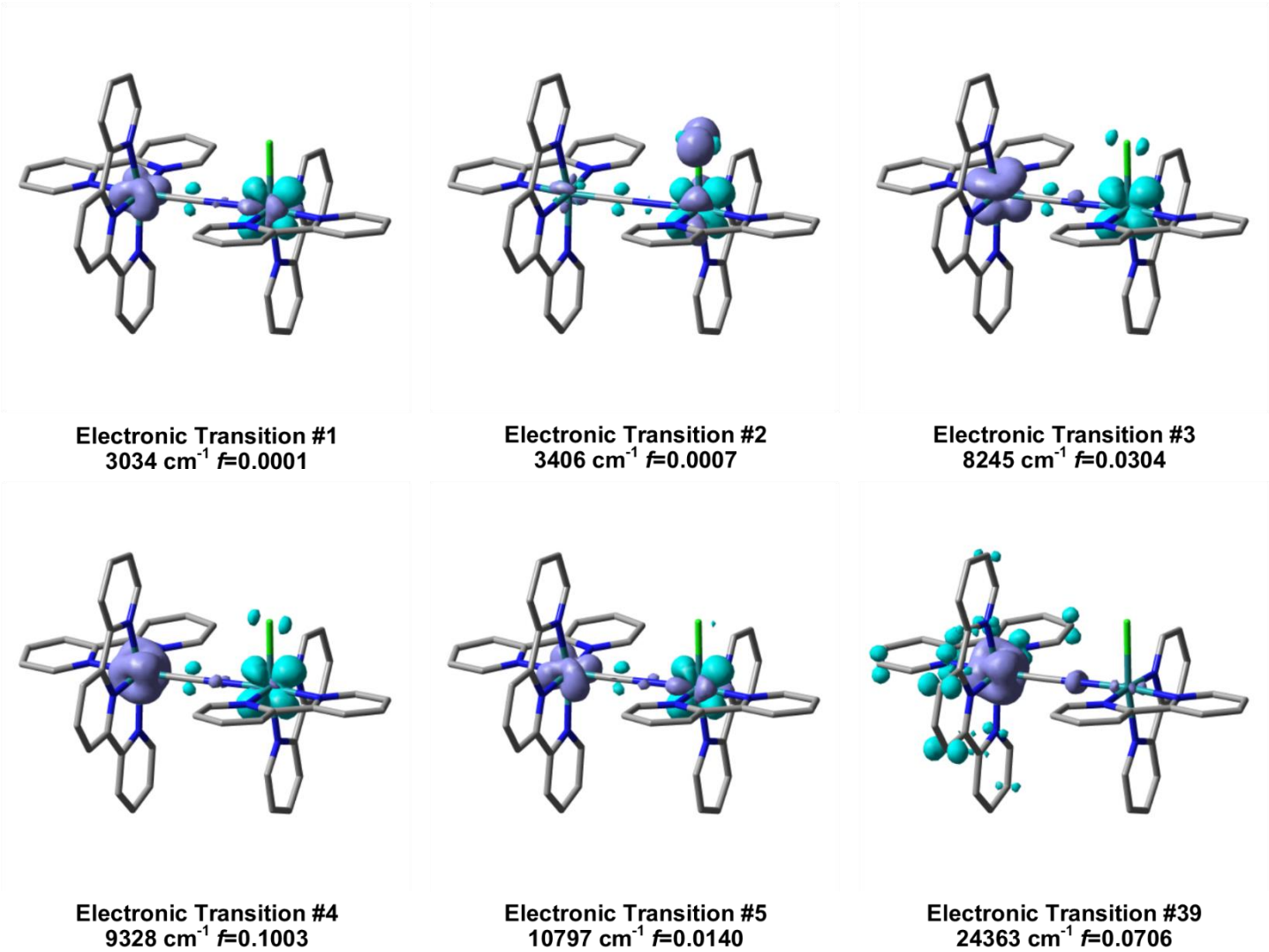

Figure S14. Electron Density Difference Maps for the selected electronic transitions of the doublet $\mathbf{1}^{3+}$ ion calculated in MeCN.

No.	Energy (cm-1)	Wavelength (nm)	Osc. Strength	Major contribs	Assignment
1	2395	4175	0.0004	H-8(B)->LUMO(B) (10%) H-3(B)->LUMO(B) (72%)	IC
2	3491	2865	0.0002	H-5(B)->LUMO(B) (34%) H-2(B)->LUMO(B) (57%)	IVCT+IC
3	7437	1345	0.0461	H-1(B)->LUMO(B) (24%) HOMO(B)->LUMO(B) (72%)	IVCT
4	8381	1193	0.0764	H-3(B)->LUMO(B) (10%) H-1(B)->LUMO(B) (70%) HOMO(B)->LUMO(B) (19%)	IVCT+IC
5	10285	972	0.0050	H-5(B)->LUMO(B) (41%) H-4(B)->LUMO(B) (13%) H-2(B)->LUMO(B) (38%)	IVCT+IC
7	13328	750	0.1262	H-5(B)->LUMO(B) (14%) H-4(B)->LUMO(B) (80%)	LMCT
39	24205	413	0.0878	H-1(A)->L+3(A) (42%) H-1(B)->L+4(B) (29%)	MLCT

Table S6. Selected electronic transitions of the doublet $\mathbf{2}^{3+}$ ion calculated in MeCN.

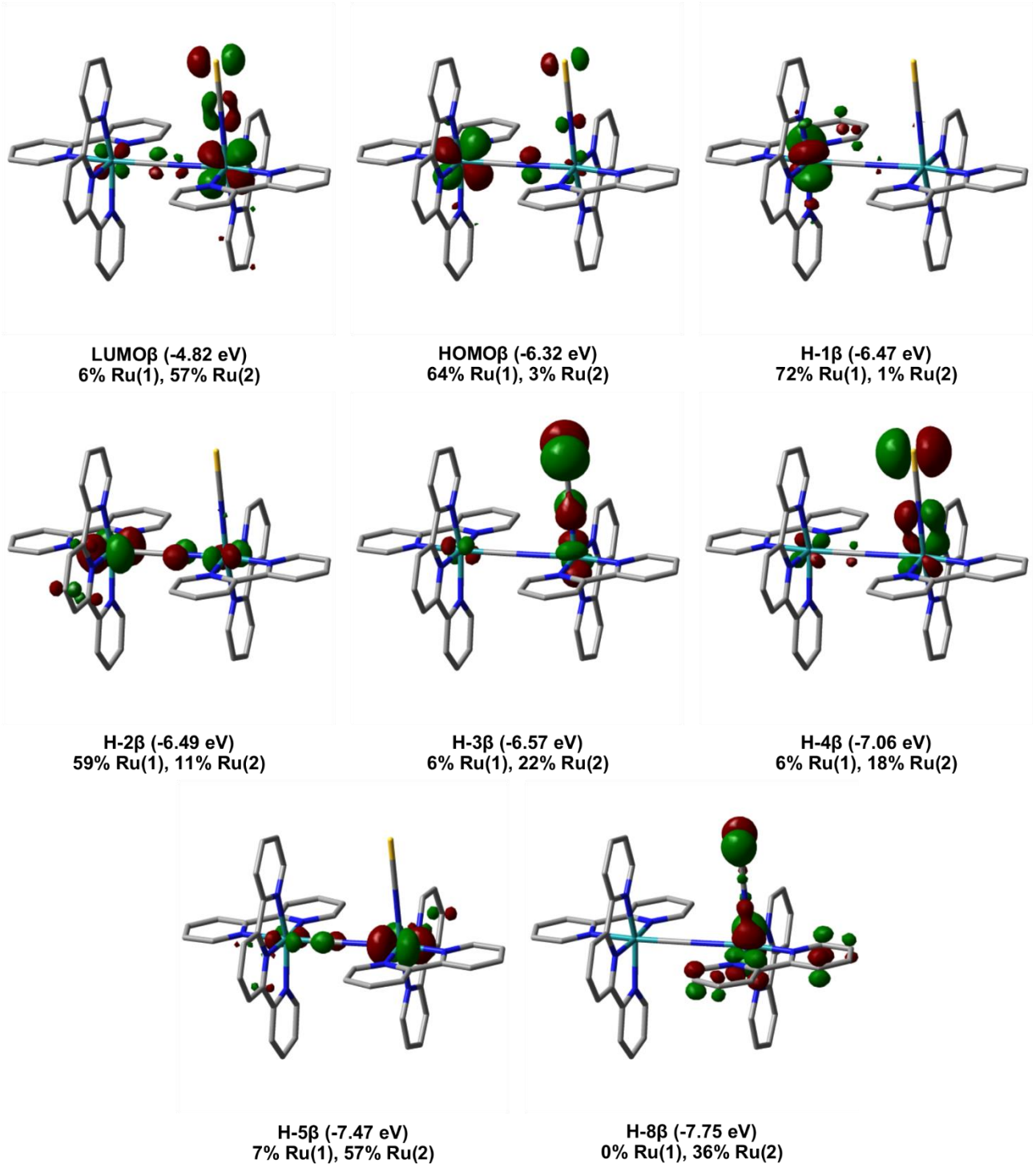

Figure S15: Computed molecular orbitals for the doublet $\mathbf{2}^{3+}$ ion calculated in MeCN.

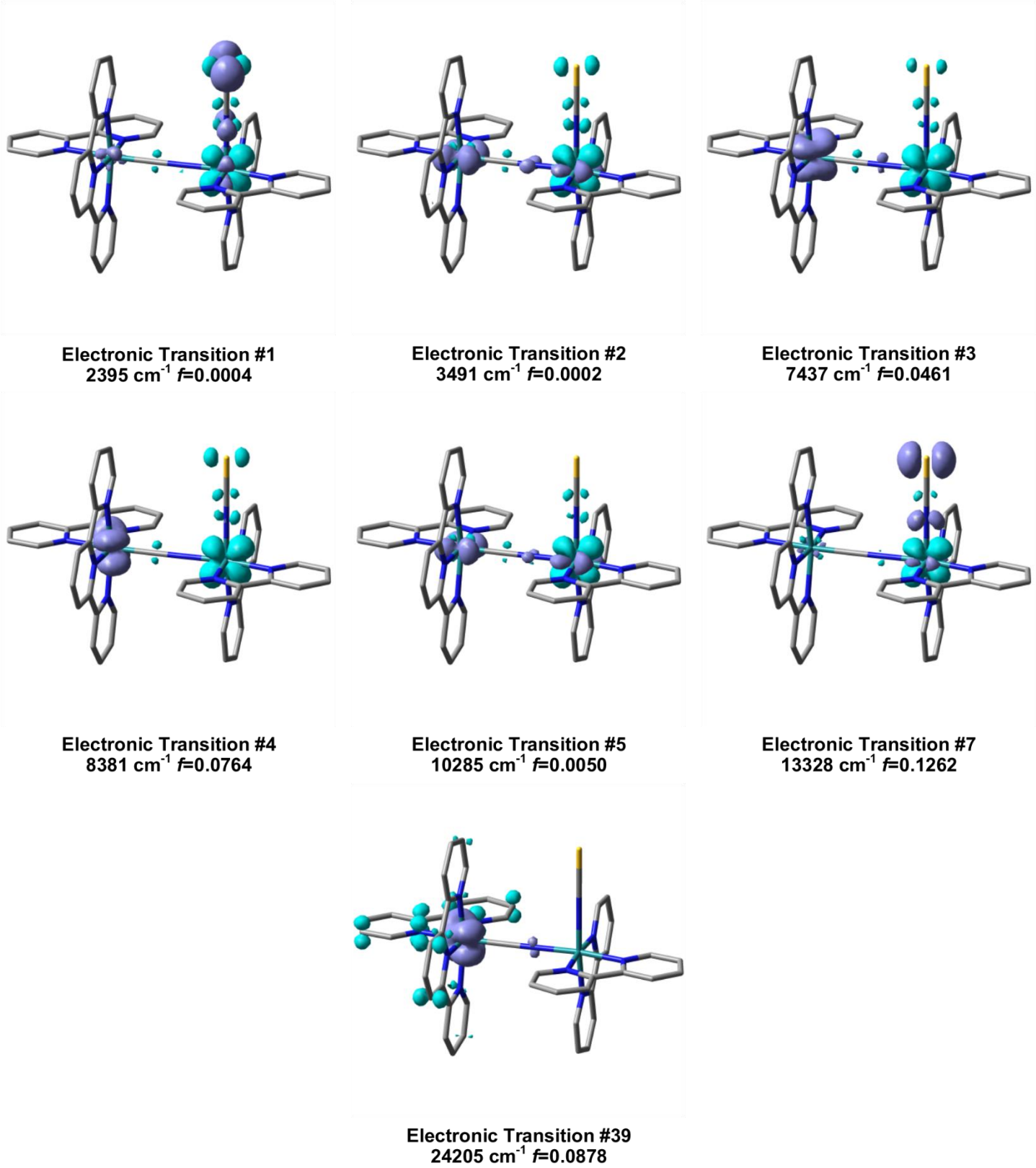

Figure S16. Electron Density Difference Maps for the selected electronic transitions of the doublet **2**$^{3+}$ ion calculated in MeCN.

No.	Energy (cm-1)	Wavelength (nm)	Osc. Strength	Major contribs	Assignment
1	2166	4616	0.0008	H-5(B)->LUMO(B) (22%) H-2(B)->LUMO(B) (27%) H-1(B)->LUMO(B) (31%)	IC
2	2592	3858	0.0058	H-5(B)->LUMO(B) (10%) H-4(B)->LUMO(B) (40%) H-3(B)->LUMO(B) (10%) HOMO(B)->LUMO(B) (28%)	IC
3	6114	1636	0.0267	H-2(B)->LUMO(B) (31%) H-1(B)->LUMO(B) (45%) HOMO(B)->LUMO(B) (18%)	IVCT+IC
4	7619	1313	0.1548	H-3(B)->LUMO(B) (37%) H-2(B)->LUMO(B) (17%) HOMO(B)->LUMO(B) (35%)	IVCT
5	9154	1092	0.0149	H-5(B)->LUMO(B) (14%) H-4(B)->LUMO(B) (36%) H-3(B)->LUMO(B) (26%) H-2(B)->LUMO(B) (16%)	IVCT+IC
6	10021	998	0.0518	H-5(B)->LUMO(B) (40%) H-3(B)->LUMO(B) (18%) H-1(B)->LUMO(B) (21%) HOMO(B)->LUMO(B) (12%)	IVCT+IC
43	25310	395	0.0469	H-2(A)->L+3(A) (18%) H-2(B)->L+4(B) (25%)	MLCT
52	26433	378	0.0316	H-3(A)->L+3(A) (12%) H-3(A)->L+4(A) (19%)	MLCT

Table S7. Selected electronic transitions of the doublet $\mathbf{3}^{4+}$ ion calculated in MeCN.

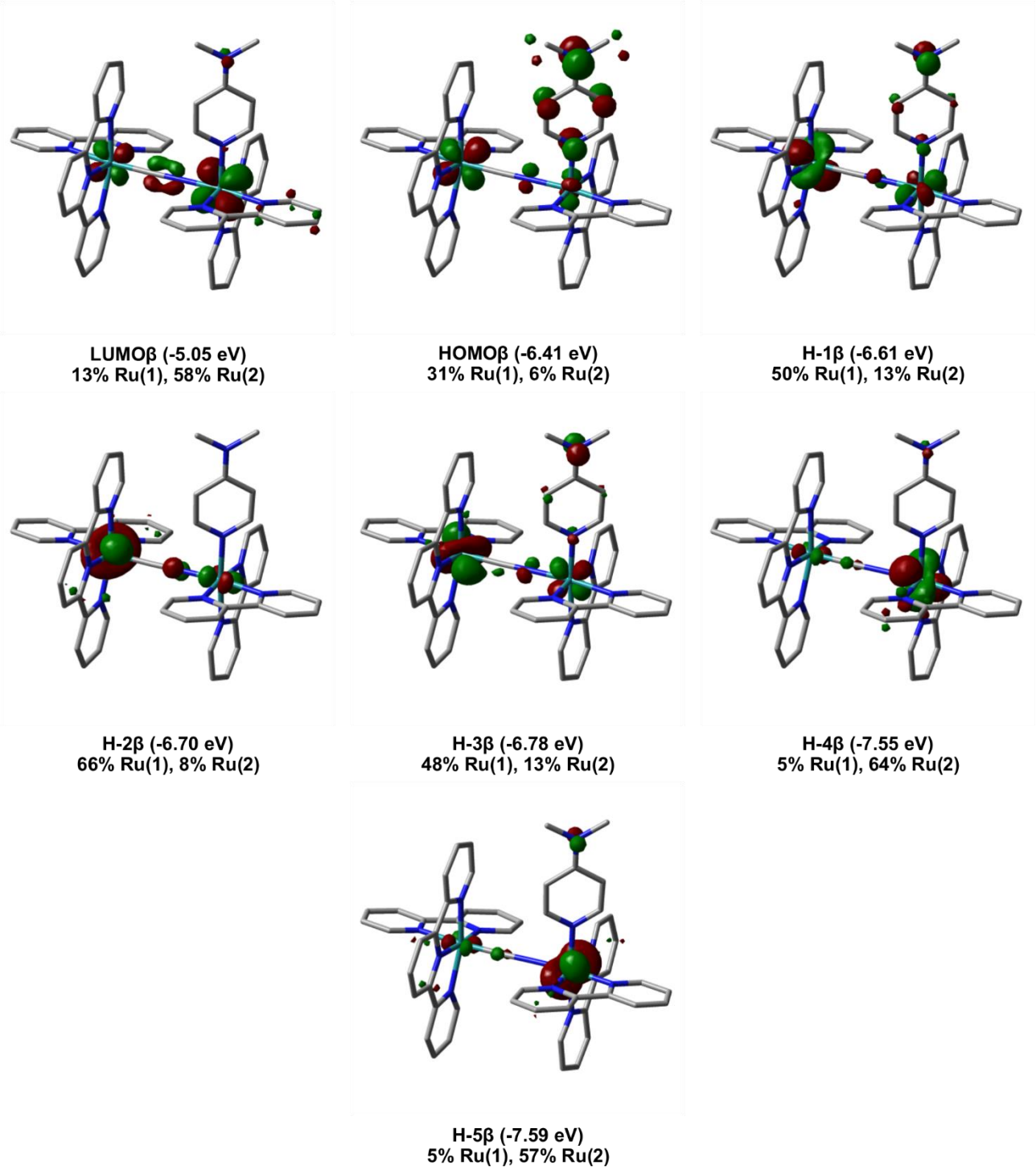

Figure S17: Computed molecular orbitals for the doublet $\mathbf{3}^{4+}$ ion calculated in MeCN.

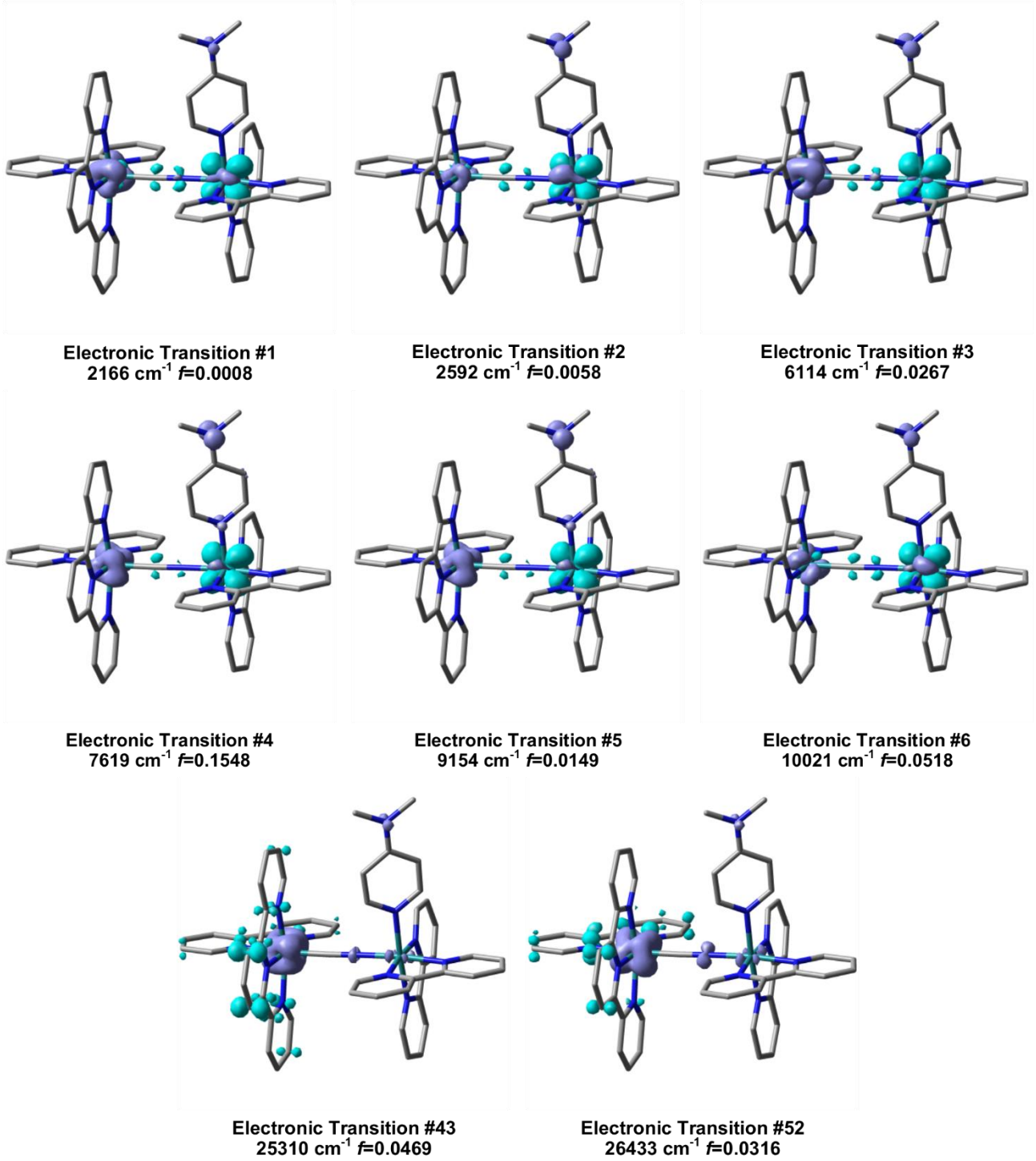

Figure S18. Electron Density Difference Maps for the selected electronic transitions of the doublet $\mathbf{3}^{4+}$ ion calculated in MeCN.

No.	Energy (cm-1)	Wavelength (nm)	Osc. Strength	Major contribs	Assignment
1	1703	5870	0.0002	H-1(B)->LUMO(B) (85%)	($d\pi_{xz}$(Ru_{1-2}) → $d\pi_{yz}$(Ru_{1-2})
2	4213	2374	0.0172	H-2(B)->LUMO(B) (65%) HOMO(B)->LUMO(B) (29%)	($d\pi_{xy}$(Ru_1) → $d\pi_{yz}$(Ru_{1-2})
3	5028	1989	0.0059	H-3(B)->LUMO(B) (86%)	($d\pi_{xy}$(Ru_2) → $d\pi_{yz}$(Ru_{1-2})
4	6839	1462	0.2456	H-2(B)->LUMO(B) (27%) HOMO(B)->LUMO(B) (60%)	($d\pi_{yz}$(Ru_{1-2}) → $d\pi_{yz}$(Ru_{1-2})
5	8080	1238	0.0073	H-4(B)->LUMO(B) (81%)	($d\pi_{xz}$(Ru_{1-2}) → $d\pi_{yz}$(Ru_{1-2})
41	26956	371	0.0432	H-1(A)->L+4(A) (10%) H-14(B)->LUMO(B) (24%) H-13(B)->LUMO(B) (26%) H-2(B)->L+4(B) (11%)	MLCT

Table S8. Selected electronic transitions of the doublet **4**$^{4+}$ ion calculated in MeCN.

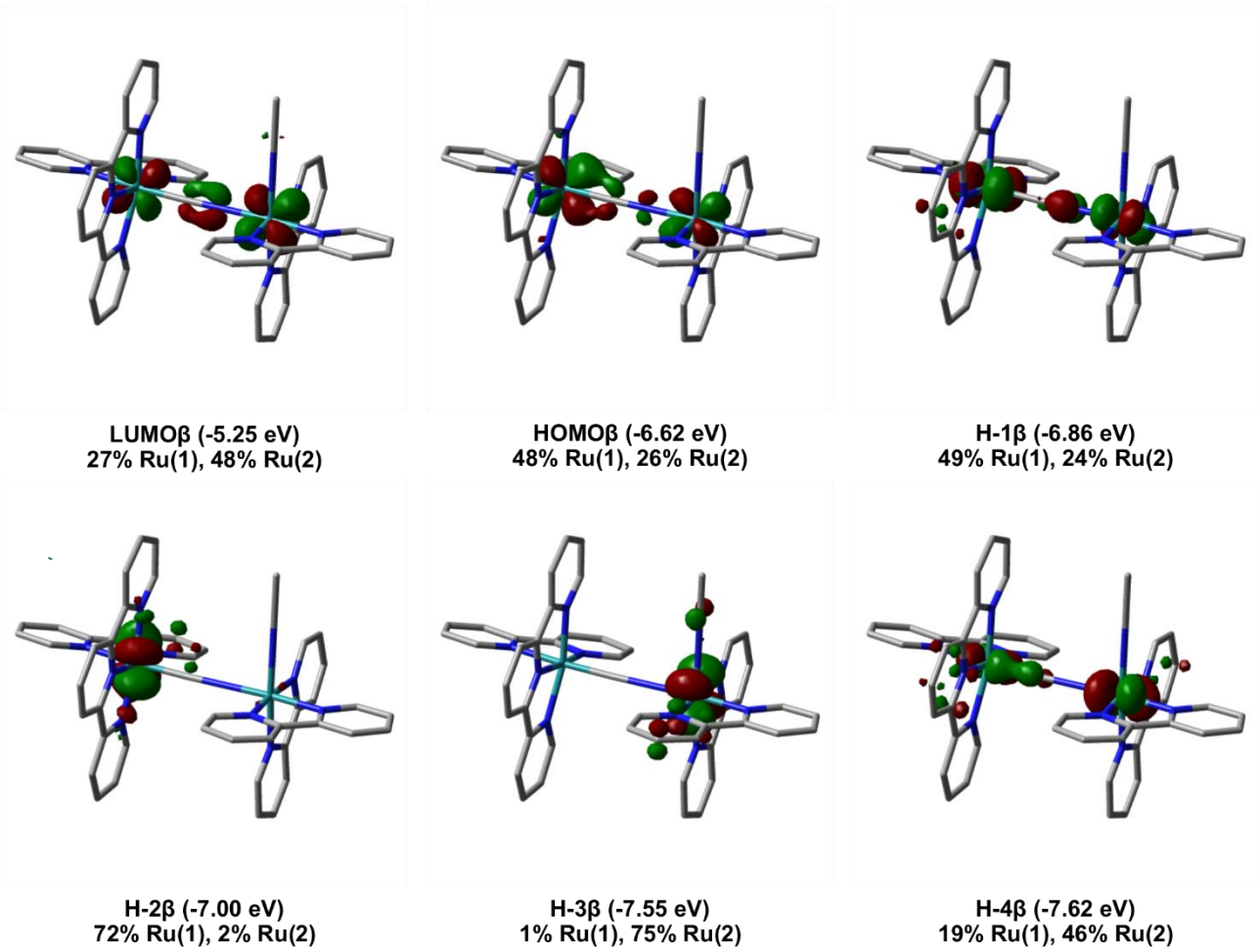

Figure S19. Computed molecular orbitals for the doublet **4**$^{4+}$ ion calculated in MeCN.

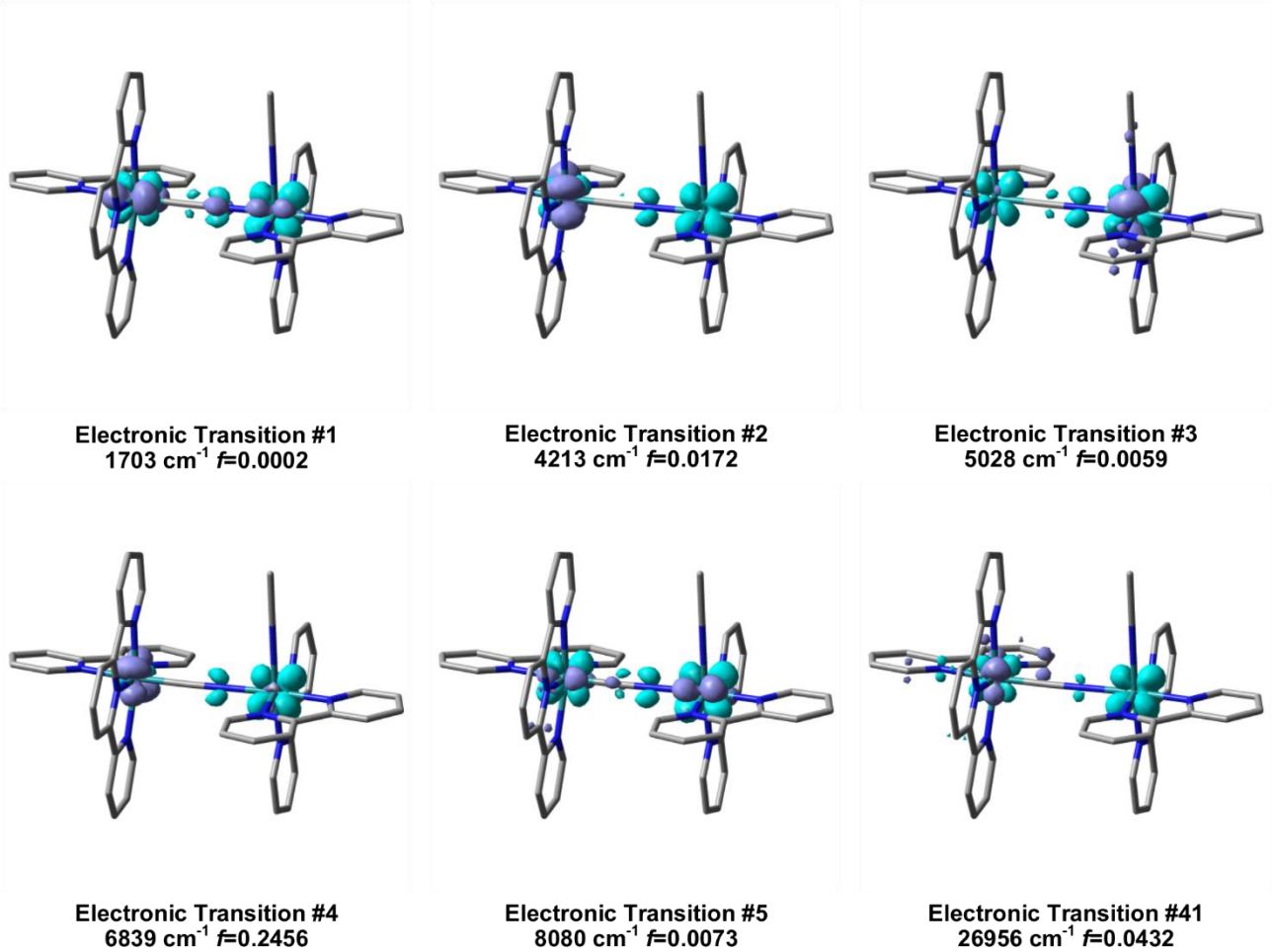

Figure S20. Electron Density Difference Maps for the selected electronic transitions of the doublet **4**$^{4+}$ ion calculated in MeCN.

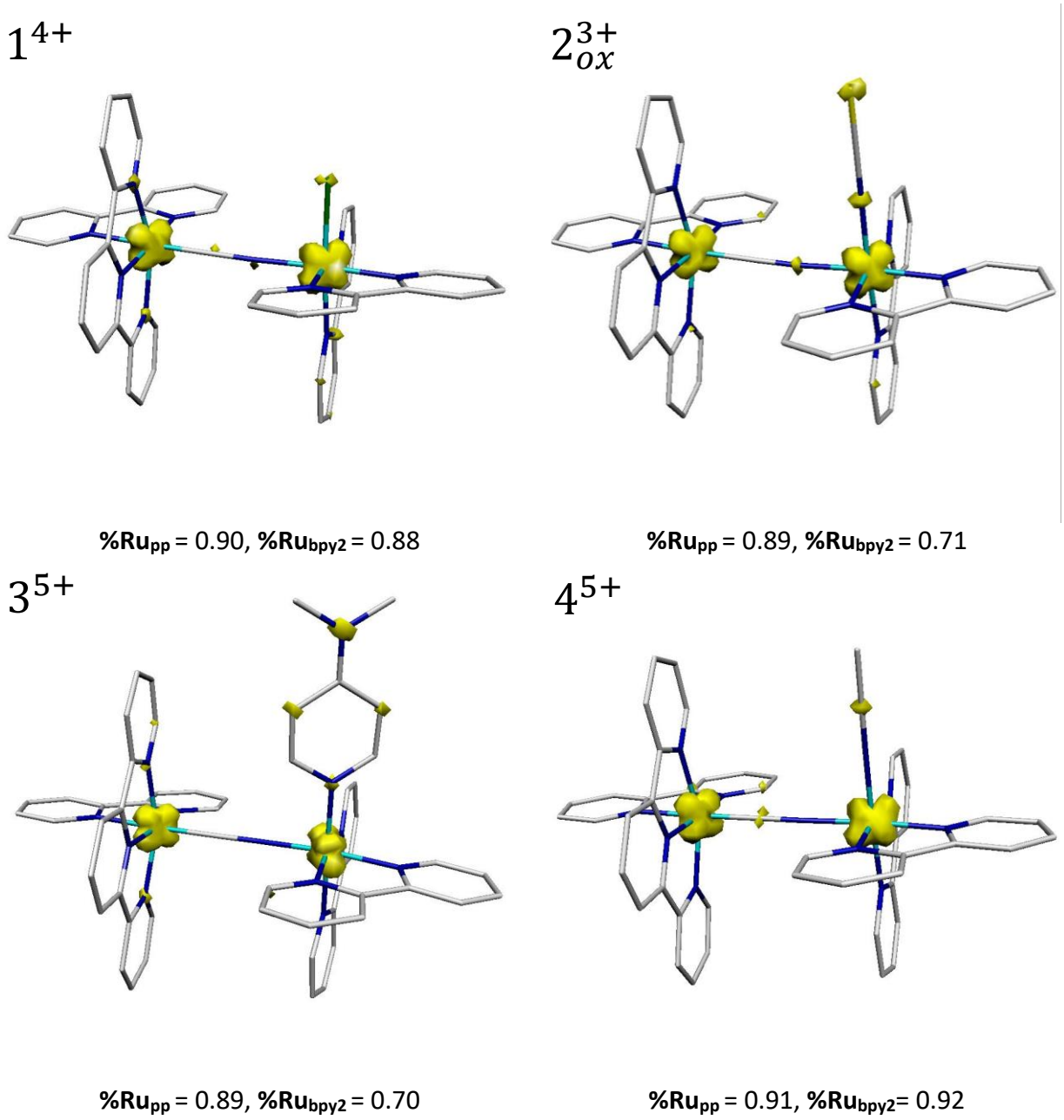

Figure S21. Computed spin density (0.02 au) and Mulliken spin density for the triplets **1**$^{4+}$, **2**$^{3+}$(ox), **3**$^{5+}$ and **4**$^{5+}$ in MeCN (IEF-PCM).